The Astrophysical Journal, 890:81 (14pp), 2020 February 10 https://doi.org/10.3847/1538-4357/ab6e6f

Large-scale Dynamics of Winds Originating from Black Hole Accretion Flows. II. Magnetohydrodynamics

Can Cui[1,2] and Feng Yuan[1,2]
[1] Shanghai Astronomical Observatory, Chinese Academy of Sciences, Shanghai 200030, People's Republic of China; ccui@shao.ac.cn
[2] University of Chinese Academy of Sciences, 19A Yuquan Road, Beijing 100049, People's Republic of China; fyuan@shao.ac.cn
Received 2019 October 29; revised 2019 December 29; accepted 2019 December 30; published 2020 February 14

Abstract

The great difference in dynamical range between small-scale accretion disk simulations and large-scale or cosmological simulations creates difficulties in tracking the disk wind kinematics. In the first paper of this series, we studied the dynamics of hydrodynamic winds from the outer edge of the accretion disk toward galactic scales. In this paper, we further incorporate magnetic fields by employing a one-dimensional magnetohydrodynamic model, with fiducial boundary conditions set for hot accretion flows. The wind solution is achieved through requiring gas to pass smoothly through the slow, Alfvén, and fast magnetosonic points. Beyond the fast magnetosonic point, physical quantities are found to show power-law dependences with cylindrical radius R, i.e., $\rho \propto R^{-2}$, $v_{\rm p} \propto$ const., $v_\phi \propto R^{-1}$, $B_\phi \propto R^{-1}$, and $\beta \propto \rho^{\gamma-1}$. The magnetization of wind is dominant in determining the wind properties. The wind is accelerated to greater terminal velocities with stronger magnetizations. The fiducial parameters result in a terminal velocity of about $0.016c$. The dependence of the wind physical quantities on temperature, field line angular velocity, and adiabatic index is also discussed.

Unified Astronomy Thesaurus concepts: Black holes (162); High energy astrophysics (739); Astrophysical black holes (98); Supermassive black holes (1663); Active galactic nuclei (16); Magnetohydrodynamics (1964); Astrophysical fluid dynamics (101)

1. Introduction

It is widely accepted that disk winds are broadly present in black hole accretion systems. On small scales, they serve as an indispensable ingredient of black hole accretion, determining the density and temperature of accretion flows, subsequently affecting the emitted spectrum (e.g., Yuan et al. 2003). On large scales, they are key to interactions and coevolution of the central black hole and its host galaxy (e.g., Ciotti et al. 2010, 2017; Ostriker et al. 2010; Choi et al. 2012; Eisenreich et al. 2017; Weinberger et al. 2017; Yoon et al. 2018, 2019; Yuan et al. 2018). Wind-launching mechanisms are extensively studied in the literature. In particular, three mechanisms have been proposed, namely, the thermally driven (e.g., Begelman et al. 1983; Font et al. 2004; Luketic et al. 2010; Waters & Proga 2012), the radiation driven (e.g., Murray et al. 1995; Proga et al. 2000; Proga & Kallman 2004; Nomura & Ohsuga 2017), and the magnetically driven winds (e.g., Blandford & Payne 1982; Lynden-Bell 1996, 2003).

The magnetohydrodynamic (MHD) wind theory has long been established, initiated by the seminal work of Blandford & Payne (1982) and Lynden-Bell (1996, 2003), followed by intense studies over the past few decades (e.g., Pudritz & Norman 1983, 1986; Sakurai 1985, 1987; Konigl 1989; Lovelace et al. 1991; Pelletier & Pudritz 1992; Cao & Spruit 1994; Contopoulos & Lovelace 1994; Ferreira & Pelletier 1995; Li 1995, 1996; Ferreira 1997; Ostriker 1997; Vlahakis et al. 2000; Everett 2005; Fukumura et al. 2010; Bai et al. 2016). Magnetically driven winds can be generally categorized into two classes, one of which is the magnetocentrifugal winds where the poloidal magnetic field dominates, and the other is winds driven by the magnetic pressure gradient, where the toroidal field dominates.

A centrifugal force is able to drive winds if the poloidal component of the magnetic fields makes an angle of more than 30° from the rotational axis (Blandford & Payne 1982). The launching of magnetocentrifugal winds generally requires the presence of a large-scale, ordered magnetic field threading the disk with a poloidal component at least comparable to the toroidal magnetic field (e.g., Cannizzo & Pudritz 1988; Pelletier & Pudritz 1992). Global MHD simulations with time-dependency have been performed to study the structure and evolution of these winds, although the internal structure of the disk is usually ignored, with winds being ejected at the boundary (e.g., Ustyugova et al. 1995, 1999; Ouyed & Pudritz 1997a, 1997b, 1999; Romanova et al. 1997; Krasnopolsky et al. 1999; Kato et al. 2002; Anderson et al. 2005; Pudritz et al. 2006; Zanni et al. 2007; Porth & Fendt 2010). The toroidal magnetic field builds up through disk rotation, giving rise to winds that are driven by the magnetic pressure gradient (Lynden-Bell 1996, 2003). Depending on the ratio of poloidal to toroidal field strength, the wind will transition from driven by magnetocentrifugal forces to driven by the magnetic pressure gradient along its propagation (Uchida & Shibata 1985; Pudritz & Norman 1986; Shibata & Uchida 1986; Stone & Norman 1994; Contopoulos 1995; Kudoh & Shibata 1997; Ouyed & Pudritz 1997b).

Global simulations on cold accretion disks suffer from proper implementation of radiative transfer processes, which is key to the thin-disk model. Moreover, the simultaneous modeling of geometrically thin disks with resolved gas dynamics and propagation of the disk winds to large radii would be prohibitively time-consuming. Previous numerical studies generally do not resolve the full internal structure of the disk. Instead, they employ simplifications by injecting winds from the simulation boundary, assuming specific wind-driving mechanism(s) (e.g., Proga et al. 2000; Proga & Kallman 2002; Luketic et al. 2010). Because the simplified model is not able to generate wind self-consistently from accretion disks, the wind properties that are obtained are not fully reliable. On the other

hand, the theoretical understanding of winds that are launched from hot accretion flows is more advanced, partly because the radiation is dynamically unimportant in hot accretion flows and it is easy to simulate geometrically thick flows. The early speculation that strong winds might exist in hot accretion flows (Narayan & Yi 1994; Blandford & Begelman 1999) was later confirmed by numerical simulations (Narayan et al. 2012; Yuan et al. 2012a, 2012b; Li et al. 2013).

Winds from hot accretion flows have been thoroughly studied in Yuan et al. (2015; hereafter Y15). They analyze data from 3D general relativistic (GR) MHD simulations via a virtual particle trajectory approach, which effectively distinguishes real wind from turbulent flows. Winds originating from smaller radii are found to have higher poloidal velocities, and the velocity roughly remains constant during the outward propagation. Differentiating from global simulations of thins disks, winds are self-consistently generated in hot accretion flow simulations with the internal dynamics of accretion flows resolved so that reliable wind properties are obtained.

The simulations mentioned above can only track winds on accretion disk scales. Nevertheless, wind properties beyond this scale are of great importance in order to understand its role in the interactions between active galactic nuclei (AGNs) and host galaxies. Recent cosmological simulations invoke winds from hot accretion flows that interact with the interstellar medium on galactic scales to overcome serious problems in galaxy formation, e.g., reducing star formation efficiency in the most massive halos (e.g., Weinberger et al. 2017). Moreover, Yuan et al. (2018) comprehensively include feedback by wind and radiation from AGNs in cold and hot feedback modes and find that wind plays a dominant role in both modes, although radiative feedback cannot be neglected.

The dynamics of disk winds have been studied in the context of black hole accretion disks with most attention paid to thin disks (e.g., Contopoulos & Lovelace 1994; Romanova et al. 1997; Proga et al. 2000; Proga 2003; Proga & Kallman 2004; Luketic et al. 2010; Waters & Proga 2012; Cao 2014; Clarke & Alexander 2016; Nomura & Ohsuga 2017; Waters & Proga 2018), and some of these works have extended to large radii. In this series, we aim to study the wind dynamics beyond accretion disk scales with an analytical method. A hydrodynamic model has been adopted in our first paper to study thermally driven winds (Cui et al. 2019). In this paper, we employ one-dimensional MHD equations to understand how magnetic fields influence the wind dynamics, with special attention to those from hot accretion flows. The key factor of studying the large-scale wind dynamics lies in the precise adoption of boundary conditions because the MHD equations controlling the wind dynamics are a set of differential equations. In this work, we revisit the large-scale dynamics with realistic boundary conditions from small-scale accretion disk simulations and focus on winds from hot accretion flows.

Analytical studies of magnetized winds in cold black hole accretion disks have been conducted in the literature. Some of these works invoke the simplification of self-similarity in solving MHD equations and therefore suffer from the fact that boundary conditions do not need to be prescribed (e.g., Everett 2005; Fukumura et al. 2010). Despite the rarity of large-scale wind studies from hot accretion flows, a recent work by Bu & Mosallanezhad (2018) investigates the wind properties of advection-dominated accretion flows via resistive MHD equations. However, their results are also limited by the adoption of self-similar solutions. In this work, we pursue the study of magnetized disk winds by the standard Weber & Davis model and solve the set of MHD equations self-consistently, with the the most realistic boundary conditions taken from small-scale accretion disk simulations (Y15).

The paper is organized as follows. We describe the MHD wind model and the analytical approach in Section 2. In Section 3 we discuss the boundary conditions in terms of hot accretion flows and thin disks. We present solutions by detailing the magnetization, temperature, mass loading, and the acceleration mechanism of the wind in Section 4. Parameter studies on adiabatic indices and disk angular velocities are conducted in Section 5. Finally, we summarize the main findings and discuss the results in Section 6.

2. Model Description and Equations

The steady ($\partial/\partial t = 0$), axisymmetric ($\partial/\partial \phi = 0$) model of magnetized disk winds is presented in this section, following equations introduced in Webber & Davis (1967). The wind geometry is prescribed in Section 2.1. The set of equations to be solved is described in Section 2.2 with the properties of critical points detailed in Section 2.3. The numerical procedures for solving MHD equations are elaborated in Section 2.4, and a sample solution is displayed in Section 2.5. We list the physical quantities in Section 2.6; this facilitates the analysis.

2.1. Wind Geometry

Using cylindrical coordinates (R, ϕ, z), we decompose the magnetic field $\boldsymbol{B}$ and velocity field $\boldsymbol{v}$ at any point in the outflow into poloidal and toroidal components,

$$\boldsymbol{B} = \boldsymbol{B}_{\rm p} + B_\phi \hat{\phi}, \quad \boldsymbol{v} = \boldsymbol{v}_{\rm p} + v_\phi \hat{\phi}, \tag{1}$$

where $\boldsymbol{v}_{\rm p}$, $\boldsymbol{B}_{\rm p}$ are the poloidal velocity and magnetic field components, v_ϕ is the rotational velocity, and B_ϕ is the toroidal magnetic field component.

The wind is prescribed to be launched from the disk surface at (R_0, z_0), known as the wind base or the footpoint of the magnetic field line. When we assume that large poloidal filed lines thread the accretion disk, the field line is anchored at the wind base and is taken to be straight for $R > R_0$ in the poloidal plane. This simplified assumption enables us to easily incorporate this in the wind geometry, and it is valid through small-scale accretion disk simulations for hot accretion flows (Y15, see their Figure 1). With a constant inclination angle θ to the rotational axis, we parameterize the poloidal filed line, which is also the streamline of the wind as a result of flux freezing, by $R = R_0 + s\cos\theta$ and $z = z_0 + s\sin\theta$, where s denotes the length along the poloidal magnetic field.

The 1D Weber and Davis model requires the prescription of the poloidal field strength along the streamline. We adopt the divergence-free condition, writing the function of $B_{\rm p}(R)$ in the form

$$B_{\rm p}(R) = B_{\rm p0}\left(\frac{R}{R_0}\right)^{-2}, \tag{2}$$

where subscript naught denotes quantities at the wind base.

2.2. Conservation Laws

A magnetized disk wind is described by six equations for six variables, the gas density ρ, pressure P, poloidal components of

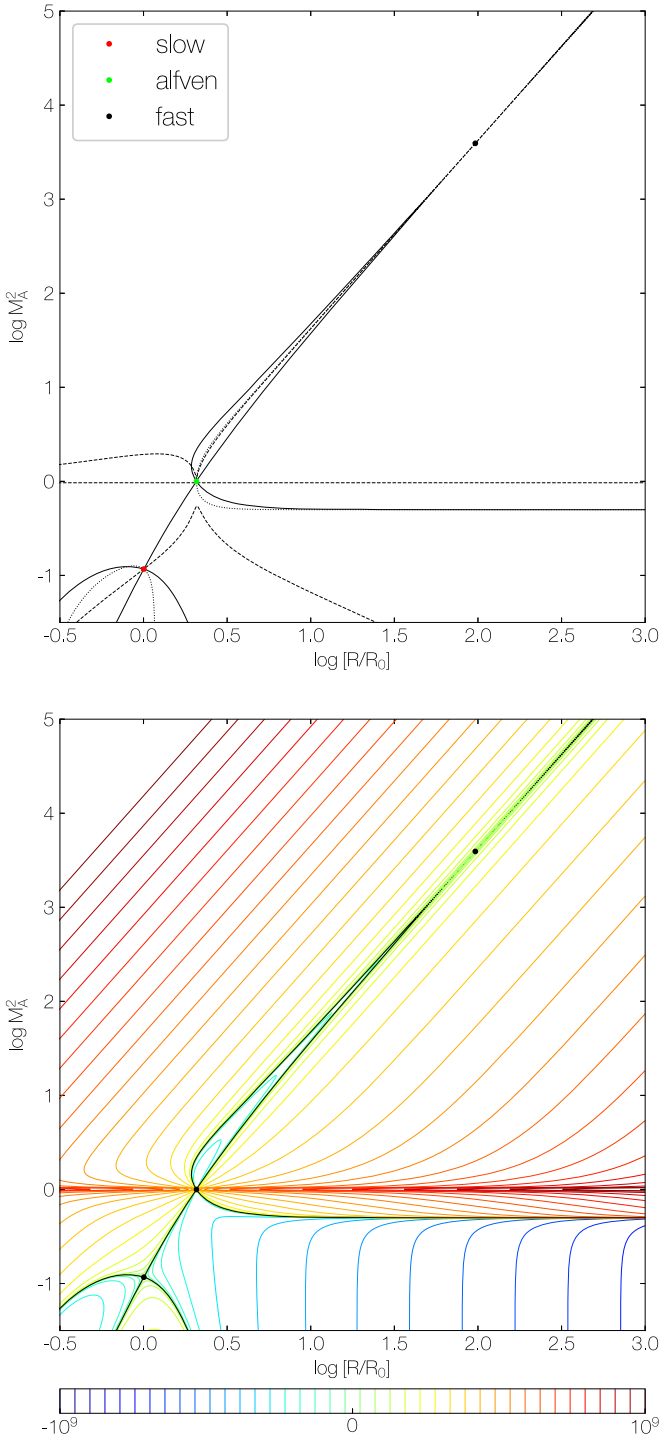

Figure 1. Solution plane of the wind model. Top panel: the solid, dashed, and dotted curves represent the solutions of $H(\rho, R) = \varepsilon$, $\partial H(\rho, R)/\partial\rho = 0$, and $\partial H(\rho, R)/\partial R = 0$. The intersections between these curves show the loci of the slow (red), Alfvén (green), and fast (black) mode velocities from the bottom to the top of the (M_A^2, R)-plane. Bottom panel: solution curves by drawing contours of $H(\rho, R)$ with Equation (19). Colors delineate deviations from $H(\rho, R) = \varepsilon$, which is highlighted in black. The wind solution should be part of the solid black curve that smoothly connects the slow, Alfvén, and fast points.

the velocity and magnetic field v_p, B_p, and toroidal components v_ϕ, B_ϕ. One of these equations prescribing the strength of the poloidal magnetic field along the streamline is shown in Equation (2). Another of these is the polytropic equation of state,

$$P = K\rho^\gamma, \tag{3}$$

where K and γ are constants, with the latter representing the polytropic index. The sound speed is defined by $c_s^2 \equiv \partial P/\partial\rho = \gamma P/\rho$. The polytropic relation is employed to express the enthalpy term in conservation of the specific energy (Equations (12) and (13)).

The remaining four Equations (9)–(12) are conservation laws derived from stationary ideal MHD. In the Gaussian unit system, these equations read (Spruit 2016)

$$\nabla\cdot(\rho\boldsymbol{v}) = 0, \tag{4}$$

$$\rho(\boldsymbol{v}\cdot\nabla)\boldsymbol{v} = -\nabla P - \rho\nabla\Phi + \frac{1}{4\pi}(\nabla\times\boldsymbol{B})\times\boldsymbol{B}, \tag{5}$$

$$\nabla\times(\boldsymbol{v}\times\boldsymbol{B}) = 0, \tag{6}$$

$$\nabla\cdot\boldsymbol{B} = 0, \tag{7}$$

where Φ represents the gravitational potential. Equation (4) is the continuity equation, and Equation (5) is the equation of motion. Equations (6) and (7) are the induction equation and the divergence-free condition that states that no magnetic monopoles exist. Owing to axisymmetry and the conservation of magnetic flux, the poloidal magnetic field is derived from the magnetic flux function ψ by Spruit (2016) and Ogilvie (2016),

$$\boldsymbol{B}_p = \frac{1}{R}\nabla\psi\times\hat{\phi}. \tag{8}$$

Hence we have $\boldsymbol{B}\cdot\nabla\psi = 0$, which indicates that the flux function ψ labels field lines or their surfaces of evolution. For steady and axisymmetric flow, Equations (4)–(7) are reduced to four conservation laws with four invariants κ, ω, l, ε. These quantities are functions of ψ, thereby they are conserved along each individual field line.

The first of these invariants can be derived from the continuity equation:

$$\kappa(\psi) \equiv \frac{4\pi\rho v_p}{B_p}, \tag{9}$$

where κ is the ratio of the mass flux to magnetic flux. The induction equation further gives the conservation of angular velocity of the filed line:

$$\omega(\psi) \equiv \frac{v_\phi}{R} - \frac{\kappa B_\phi}{4\pi\rho R}, \tag{10}$$

where $v_\phi = \Omega R$, and Ω is the gas angular velocity. Following Equation (6), the steady and axisymmetric conditions give $\boldsymbol{v}_p\times\boldsymbol{B}_p = 0$ bcause ethey do not allow the existence of a toroidal electric field ($\boldsymbol{E}_\phi = -v_p\times B_p/c = 0$). Thus, the poloidal velocity and magnetic field are everywhere parallel to each other, $\boldsymbol{v}_p\|\boldsymbol{B}_p$. This expresses the flux-freezing condition and does not depend on the reference frames. Along with Equation (10), the total gas velocity is parallel to the total magnetic field in the frame rotating with ω. The azimuthal component of the equation of motion implies the conservation of angular momentum on each filed line:

$$l(\psi) \equiv v_\phi R - \frac{RB_\phi}{\kappa}. \tag{11}$$

The first term on the right is the ordinary specific angular momentum, and the second term represents the torque associated with the magnetic stresses. The Bernoulli integral or the conservation of specific energy expresses the last invariant:

$$\varepsilon(\psi) \equiv \frac{1}{2}v_{\rm p}^2 + \frac{1}{2}(v_\phi - \omega R)^2 + \Phi_{\rm eff} + h, \tag{12}$$

where $\Phi_{\rm eff} = \Phi - \omega^2 R^2/2$ is the combined potential energy of centrifugal and gravitational forces along the field line. The gravitational potential by a point mass is defined as $\Phi = -GM_{\rm BH}(R^2 + z^2)^{-1/2}$, where $M_{\rm BH}$ is the mass of the central black hole. Along with the polytropic law, the enthalpy $h = \int dP/\rho$ is written as

$$h = \frac{\gamma}{\gamma - 1} K\rho^{\gamma - 1}. \tag{13}$$

It is obvious from the angular velocity and centrifugal potential terms that Equation (12) is written in the rotating frame with the footpoint angular velocity ω. In the rest frame, the Bernoulli constant is given by $\tilde{\varepsilon} = v^2/2 + \Phi + h - R\omega B_\phi/\kappa$, where $v = (v_{\rm p}^2 + v_\phi^2)^{1/2}$. The last term corresponds to the Poynting flux and is not shown in ε. This is because in the rotating frame, the magnetic field is strictly parallel to the flow velocity such that the Lorentz force $\mathrm{F_L} = \boldsymbol{J} \times \boldsymbol{B}/c$ everywhere perpendicular to $\boldsymbol{B}$ is perpendicular to $\boldsymbol{v} - \omega R\hat{\phi}$, hence the field does no work in this frame. The two Bernoulli integrals are related by $\varepsilon = \tilde{\varepsilon} - l\omega$.

2.3. Critical Points

It is convenient to introduce the poloidal Alfvénic Mach number $M_{\rm A}$, which is defined as

$$M_{\rm A}^2 = \frac{v_{\rm p}^2}{v_{\rm Ap}^2} = \frac{\kappa^2}{4\pi\rho}, \tag{14}$$

where $v_{\rm Ap} = B_{\rm p}/\sqrt{4\pi\rho}$ is the poloidal Alfvén velocity. Eliminating B_ϕ in Equations (10) and (11) gives

$$v_\phi = \frac{M_{\rm A}^2 l/R - \omega R}{M_{\rm A}^2 - 1}. \tag{15}$$

The radius $R = R_{\rm A}$ where $M_{\rm A} = 1$ is the Alfvénic point. The denominator of the expression for v_ϕ goes to zero at this point, hence we require the numerator to vanish identically. This results in a simple expression for the conserved specific angular momentum as

$$l = \omega R_{\rm A}^2. \tag{16}$$

Substituting Equations (9)–(11) into Equation (12), the Bernoulli integral, we can express ε as a function of ρ and R,

$$\varepsilon = H(\rho, R), \tag{17}$$

and $H(\rho, R)$ takes the explicit expression

$$H(\rho, R) = \frac{1}{2}\frac{\kappa^2 B_{\rm p}^2}{(4\pi\rho)^2} + \frac{1}{2}\frac{(l/R - \omega R)^2\kappa^4}{(4\pi\rho - \kappa^2)^2} + \Phi_{\rm eff} + h. \tag{18}$$

Substituting ρ by $M_{\rm A}$ through Equation (19), we obtain

$$H(M_{\rm A}, R) = \frac{1}{2}\frac{M_{\rm A}^4 B_{\rm p}^2}{\kappa^2} + \frac{1}{2}\frac{(l/R - \omega R)^2}{(M_{\rm A}^{-2} - 1)^2} + \Phi_{\rm eff} + h. \tag{19}$$

Critical points can be obtained by requiring the partial derivatives of $H(\rho, R)$ to be zero,

$$\frac{\partial H(\rho, R)}{\partial \rho} = \frac{\partial H(\rho, R)}{\partial R} = 0, \tag{20}$$

which gives the slow ($\rho_{\rm s}$, $R_{\rm s}$) and the fast ($\rho_{\rm f}$, $R_{\rm f}$) magnetosonic point. The subscripts s and f denote the slow and fast critical points. In particular, these points manifest themselves in the partial derivative of ρ,

$$\begin{aligned}\rho\frac{\partial H}{\partial \rho} &= -v_{\rm p}^2 - \frac{(\Omega - \omega)^2 R^2}{1 - M_{\rm A}^2} + c_{\rm s}^2 \\ &= \frac{v_{\rm p}^4 - (c_{\rm s}^2 + v_{\rm Ap}^2 + v_{{\rm A}\phi}^2)v_{\rm p}^2 + c_{\rm s}^2 v_{\rm Ap}^2}{v_{\rm Ap}^2 - v_{\rm p}^2} \\ &= \frac{(v_{\rm p}^2 - v_{\rm sp}^2)(v_{\rm p}^2 - v_{\rm fp}^2)}{v_{\rm Ap}^2 - v_{\rm p}^2},\end{aligned} \tag{21}$$

where $v_{{\rm A}\phi} = B_\phi/\sqrt{4\pi\rho}$ is the toroidal Alfvén velocitiy, and the square of the sound speed is defined as $c_{\rm s}^2 \equiv \partial P/\partial\rho = \gamma P/\rho$. The expressions of $v_{\rm sp}$ and $v_{\rm fp}$ are given by the quadratic formula

$$v_{\rm sp}^2,\, v_{\rm fp}^2 = \frac{(c_{\rm s}^2 + v_{\rm A}^2) \mp \sqrt{(c_{\rm s}^2 + v_{\rm A}^2)^2 - 4c_{\rm s}^2 v_{\rm Ap}^2}}{2}, \tag{22}$$

where $v_{\rm A}^2 = v_{\rm Ap}^2 + v_{{\rm A}\phi}^2$. The left-hand side vanishes in Equation (21) when $v_{\rm p}$ equals either the slow-mode velocity $v_{\rm sp}$ or the fast-mode velocity $v_{\rm fp}$. In addition to the conditions for critical points imposed by Equation (20), a further constraint is placed to equate the energies at slow and fast points to the Bernoulli constant,

$$H(\rho_{\rm s}, R_{\rm s}) = \varepsilon, \qquad H(\rho_{\rm f}, R_{\rm f}) = \varepsilon. \tag{23}$$

We have seen that at the slow and fast magnetosonic points six equations are introduced, i.e., Equations (20) and (23) at ($\rho_{\rm s}$, $R_{\rm s}$) and ($\rho_{\rm f}$, $R_{\rm f}$), while eight variables ($\rho_{\rm s}$, $R_{\rm s}$, $\rho_{\rm f}$, $R_{\rm f}$, κ, ω, l, ε) are presented. If two of these variables are specified, then the remaining six can be determined. In this paper, we fix ω and ε, and solve for the remaining variables $\rho_{\rm s}$, $R_{\rm s}$, $\rho_{\rm f}$, $R_{\rm f}$, κ and l. Hence, any wind solution is characterized by ω and ε.

2.4. Numerical Procedures

We have verified that in a pure hydrodynamic model, wind solutions should be either supersonic or transonic, whereas the subsonic solutions are not likely to exist because of low-frequency acoustic perturbations (Cui et al. 2019). Our MHD equations are accordingly solved under the condition that all solutions smoothly pass through the slow, Alfvén, and fast magnetosonic point. The general equations to be solved are given in Equations (20) and (23). These equations must be fulfilled at the slow and fast magnetosonic point. To start with, we iterate over a set of values for l and solve for κ, $R_{\rm s}$, $M_{\rm As}^2$ at the slow critical point. We then solve for l, $R_{\rm f}$, $M_{\rm Af}^2$ at the fast critical point using κ found at the slow point. The initial guess

of l and its computed value at fast point are compared for each iteration until the two values match. The initial guesses for all these variables are taken through the inspection of the contour $H(\rho, R) = \varepsilon$. Once ρ_s, R_s, ρ_f, R_f, κ and l are found, the remaining variables can be obtained by either solving $H(\rho, R) = \varepsilon$ directly or tracking along the contour curve.

Success in finding the solution at the first time involves difficulties. However, once the first set of solution is achieved, it can be used as the initial guess as we alter the parameters to find new sets of solutions. Note that the initial poloidal velocities of some solutions exceed the slow-mode velocities, or equivalently, $R_s < R_0$. The wind can be accelerated through any other mechanism when $R < R_0$, which is beyond the scope of this paper, and we focus on the large-scale wind dynamics for $R > R_0$ in the ideal MHD regime in the model established in this paper.

2.5. Solution Plane

Figure 1 shows the solution plane of the wind model. In the top panel, we plot curves of $H(\rho, R) = \varepsilon$, $\partial H(\rho, R)/\partial\rho = 0$, and $\partial H(\rho, R)/\partial R = 0$ in the (M_A^2, R) plane. Their interactions represent the slow, Alfvén, and fast magnetosonic points, respectively. The wind solution curve is part of the solid curve that smoothly connects the slow, Alfvén, and fast magnetosonic point in order, and the poloidal flow velocity exceeds the slow-, Alfvén-, and fast-mode velocities when the solution crosses the corresponding critical points.

In the bottom panel, we plot the contours of $H(\rho, R)$ and highlight the $H(\rho, R) = \varepsilon$ curve in black in which our wind solution resides, using Equation (19). The colors delineate contours with Bernoulli integrals that deviate from ε. Inspecting the color contours near the critical points shows that the slow and fast critical points are saddle points. Although the Alfvén point is a focus of a bundle of cruves, it does not impose additional constraints on the wind solution. This can be understood because the condition has already been applied at the Alfvén point in deriving Equation (16). Strictly speaking, it should be referred to the Alfvén point, but not to the Alfvén critical point.

2.6. Definition of Physical Quantities

The Alfvén point separates the wind solution into two regimes in terms of rotation. For $M_A \ll 1$, Equation (15) gives

$$v_\phi \approx \omega R, \tag{24}$$

where the fluid corotates ($\Omega = \omega$) with the angular velocity of the magnetic field lines. For $M_A \gg 1$,

$$v_\phi \approx \frac{l}{R}, \tag{25}$$

and the fluid rotates by conserving its specific angular momentum. In practice, wind usually starts from low velocities ($M_A \ll 1$) so that we can identify $\omega \approx \Omega_0$, where Ω_0 is the angular velocity of the wind at the footpoint. The specific angular momentum is $\Omega_0 R_0^2$ at the launching point. Once the wind is accelerated to the Alfvén point, the excess of the specific angular momentum is $\Omega_0(R_A^2 - R_0^2)$. By the assumption that $\Omega_0 \approx \Omega_K(R_0)$, the wind mass-loss rate is related to the mass accretion rate inside the disk according to Ferreira & Pelletier (1995) and Bai et al. (2016)

$$\xi = \frac{1}{\dot{M}_{acc}}\frac{d\dot{M}_{wind}}{d\ln R} = \frac{1}{2}\frac{1}{(R_A/R_0)^2 - 1}, \tag{26}$$

where $\dot{M}_{acc}$ is the wind-driven accretion rate, $\dot{M}_{wind}(R)$ is the cumulative mass-loss rate, ξ is called the ejection index, and the ratio R_A/R_0 is often referred to as the magnetic lever arm. The location of the Alfvén point can thereby provide a convenient measure of the mass loss to the accretion rate.

To quantify the wind properties, we introduce the dimensionless mass-loading parameter μ, defined as

$$\mu = \kappa\frac{\omega R_0}{B_{p0}}. \tag{27}$$

The invariant κ in Equation (9) represents the mass flux per field line. The mass-loading parameter is obtained by normalizing κ with $B_{p0}/\omega R_0$. The wind is lightly loaded when $\mu \ll 1$, and heavily loaded when $\mu \gg 1$. Characteristic quantities of the wind can be written explicitly as a function of μ in a simplified model (Equations (28)–(30)), which assumes that wind propagates along the equatorial plane and ignores thermal pressure ($c_s = 0$; Spruit 2016). Our wind model has a more general application than the simplified model and differs from it by a constant angle from the equatorial plane and finite wind temperature. In Section 4.5 we directly compare our results to the expressions derived from this simplified model.

The locus of the Alfvén point can be expressed as

$$\frac{R_A}{R_0} = \left[\frac{3}{2}(1 + \mu^{-2/3})\right]^{1/2}. \tag{28}$$

As the wind is lightly loaded, the Alfvén radius is far from the wind base. While for heavily loaded wind, the Alfvén radius reaches a minimum of $R_A/R_0 = (3/2)^{1/2}$ when $\mu \to \infty$. Furthermore, the terminal wind velocity can be written as

$$v_p^\infty = \omega R_0 \mu^{-1/3}, \tag{29}$$

which states that wind carrying low-mass flux can be accelerated to high velocities. When $\mu = 1$, the terminal velocity is equal to the rotational velocity at the wind base.

The ratio of the toroidal to poloidal magnetic field at the Alfvén radius can be approximated by

$$\left.\frac{B_\phi}{B_p}\right|_{R_A} \approx (19/8)^{1/2} \quad (\mu \ll 1),$$
$$\approx 1.14\mu \qquad (\mu \gg 1). \tag{30}$$

In the limit of weak mass-loading, the ratio reaches a constant and is nearly unity. This case can be referred to as the centrifugally accelerated wind. Up to the Alfvén radius, the field lines are not strongly bent and the wind corotates with the field line. At the other limit, with strong mass-loading, the field line winds up, developing a strong toroidal magnetic field from the wind base with the corotation breaking down. The wind is then accelerated by the toroidal magnetic pressure gradient, and the terminal velocity is much lower than that at the wind base.

Another quantity of interest is the ratio of the Poynting flux to the kinetic energy flux σ. The component of the Poynting flux parallel to the poloidal field is $-\omega R B_p B_\phi/4\pi$. Far beyond

the Alfvén radius $R \gg R_A$, we expect $\Omega \approx \omega R_A^2/R^2$ by Equation (15) so that $\Omega \ll \omega$. Thereby, from Equation (10), we have $B_p \approx B_\phi v_p/\omega R$, hence $B_\phi \gg B_p$ at very large R. Then, we can write the conversion of magnetic to kinetic energy as

$$\sigma = \frac{-\omega R B_p B_\phi}{2\pi\rho v_p^3} \approx \frac{B_\phi^2}{2\pi\rho v_p^2}\Bigg|_\infty \approx 2\frac{v_A^2}{v_p^2}\Bigg|_\infty . \quad (31)$$

Note that at infinity, we have $v_p > v_A$ because $v_{fp} > v_A$, which gives an asymptotic value of $\sigma < 2$.

3. Model Parameters

The footpoint of the magnetized disk winds is set to be at a spherical radius $r_0 = 10^3 r_g$, where $r_g \equiv GM/c^2$ is the gravitational radius. For convenience, we normalize radius, velocity, and density by their values at the footpoint of the field line, such that $R_0 = v_{K0} = \rho_0 = 1$. The poloidal magnetic field strength is parameterized by the poloidal Alfvén velocity $v_{Ap0} = B_{p0}/\sqrt{4\pi\rho_0}$ at the wind base. This conveniently relates the magnetic field strength to the velocity so that we can describe the field strength by comparing it to the Keplerian velocity. For the fiducial wind model, the parameters are chosen to be

$$\begin{aligned} &z_0 = 0.5R_0, \quad && \theta = 45^\circ, \\ &v_{Ap0} = 0.2v_{K0}, \quad && c_{s0} = 0.5v_{K0}, \quad && \omega = 0.8\Omega_{K0}, \end{aligned} \quad (32)$$

and the adiabatic index is set to $\gamma = 1.4$ throughout.

The fiducial parameters are set by considering the regime of hot accretion flows. Wind properties are investigated in Y15 based on 3D GRMHD simulations where disk winds are produced self-consistently from hot accretion flows. These winds are launched from $\sim 30 r_g$ up to the outer boundary of the accretion flow, which implies that at the footpoint, winds are a combination of those originating from $r \leqslant r_0$. Launched from different radii, winds possess different velocities and almost remain constant during the outward propagation, indicating that the velocity at the footpoint must be diverse. The trajectory of wind after launch is found to follow a straight line along an angle $\theta \lesssim 45^\circ$, i.e., it is more prone to the pole rather than the equatorial plane.

We adopt the wind properties that were reported in Y15 as our fiducial model parameters. The location of the footpoint is chosen to be the outer radial boundary of their simulations. The hot accretion flow maintains a disk aspect ratio whose scale height H is about a half of the cylindrical radius R. We assume that the wind base is at one disk scale height and set $\theta = 45^\circ$ in the fiducial model. The poloidal magnetic field strength v_{Ap0} is adopted so that the plasma $\beta \equiv P_{gas}/P_{mag} = 8\pi\rho c_s^2/(B_p^2 + B_\phi^2)$, defined as the gas pressure over magnetic pressure, is about unity at the wind base (Figure 2). The sound speed is set by the disk aspect ratio $H/R = c_{s0}/v_{K0}$, which is equivalent to about 1.36×10^9 K at the footpoint. The fiducial angular velocity of the field line ω is computed by Equation (10) in accretion disk simulations. We note that the poloidal velocity at the footpoint is not prescribed in Equation (32), different from our previous hydrodynamic work, because satisfying conditions of passing through all three critical points smoothly places constraints on the number of parameters that need to be given. Hence, the poloidal velocity v_{p0} is solved by MHD equations, and we confirm that the value found in the fiducial setup is consistent with the value of GRMHD simulations (see Section 4.2).

Winds that emerged from thin disks have different properties from hot accretion flows. The disks are cold, for which situation the sound speed c_{s0} is expected to be low. A value of 0.1 or $0.05v_{K0}$ is usually taken for these disks in numerical simulations. For both accretion regimes, the magnetic field strengths at the wind base are barely constrained. Aiming to include a variety of winds with diverse properties from hot accretion flows and thin disks, we employ parameter spaces as follows in addition to our fiducial setup. We obtain wind solutions over large domains of the poloidal magnetic field, where $v_{Ap0} \in [0.01, 100]$. The temperatures at the wind base span over $c_{s0} \in [0.01, 0.5]$. The angular velocity of the field line $\omega \in \{0.8, 1\}$ and the adiabatic index $\gamma \in \{1.3, 1.4, 1.5\}$ are also investigated in Section 5.

4. Results

In this section we present numerical results of MHD wind solutions by analyzing the fiducial model in Section 4.1, the dependence on the poloidal magnetic field strength in Section 4.2, the wind temperature in Section 4.3, and the mass loading in Section 4.5. The wind acceleration mechanism is discussed in Section 4.4. We note that all the solutions obtained have sub-Alfvénic velocities at the wind base, although some of the solutions may already pass through the slow magnetosonic point.

4.1. The Fiducial Solution

We commence with analyzing the behavior of characteristic physical quantities with the fiducial parameters prescribed in Equation (32), shown by curves of $v_{Ap0} = 0.2$ in Figure 2. The radial profiles of the density, the poloidal and toroidal velocities, the ratio of the magnetic field, plasma β, and the ratio of the Poynting to kinetic energy flux are displayed in the plot.

The upper middle panel indicates that the wind is accelerated monotonically by passing through the Alfvén and fast magnetosonic points. We note that the poloidal velocities of the fiducial model already passed through the slow magnetosonic point at the wind base. The wind continues to accelerate after propagating through the Alfvén point. The poloidal velocity approaches an asymptotic value at large radii; beyond the fast point, it almost remains constant. From the figure, the density profile drops as $\rho \propto R^{-2}$ at large distances, which is as expected in Equation (9) because the poloidal magnetic field strength is prescribed to obey the divergence-free condition as $B_p \propto R^{-2}$, and the poloidal velocity remains about constant beyond the fast point.

The angular velocity profile shown in the upper right panel shows whether the gas corotates with the field line, i.e., $v_\phi \propto R$, or rotates by conserving its specific angular momentum, i.e., $v_\phi \propto R^{-1}$. These two regimes correspond to different wind acceleration mechanisms that are detailed in Section 4.4. In short, when the poloidal magnetic field dominates the toroidal component, corotation occurs and is associated with the magnetocentrifugal force. During the outward propagation of the gas, the field lines wind up with the development of toroidal magnetic fields. Corotation ceases when the toroidal component dominates. The wind then rotates by conserving the

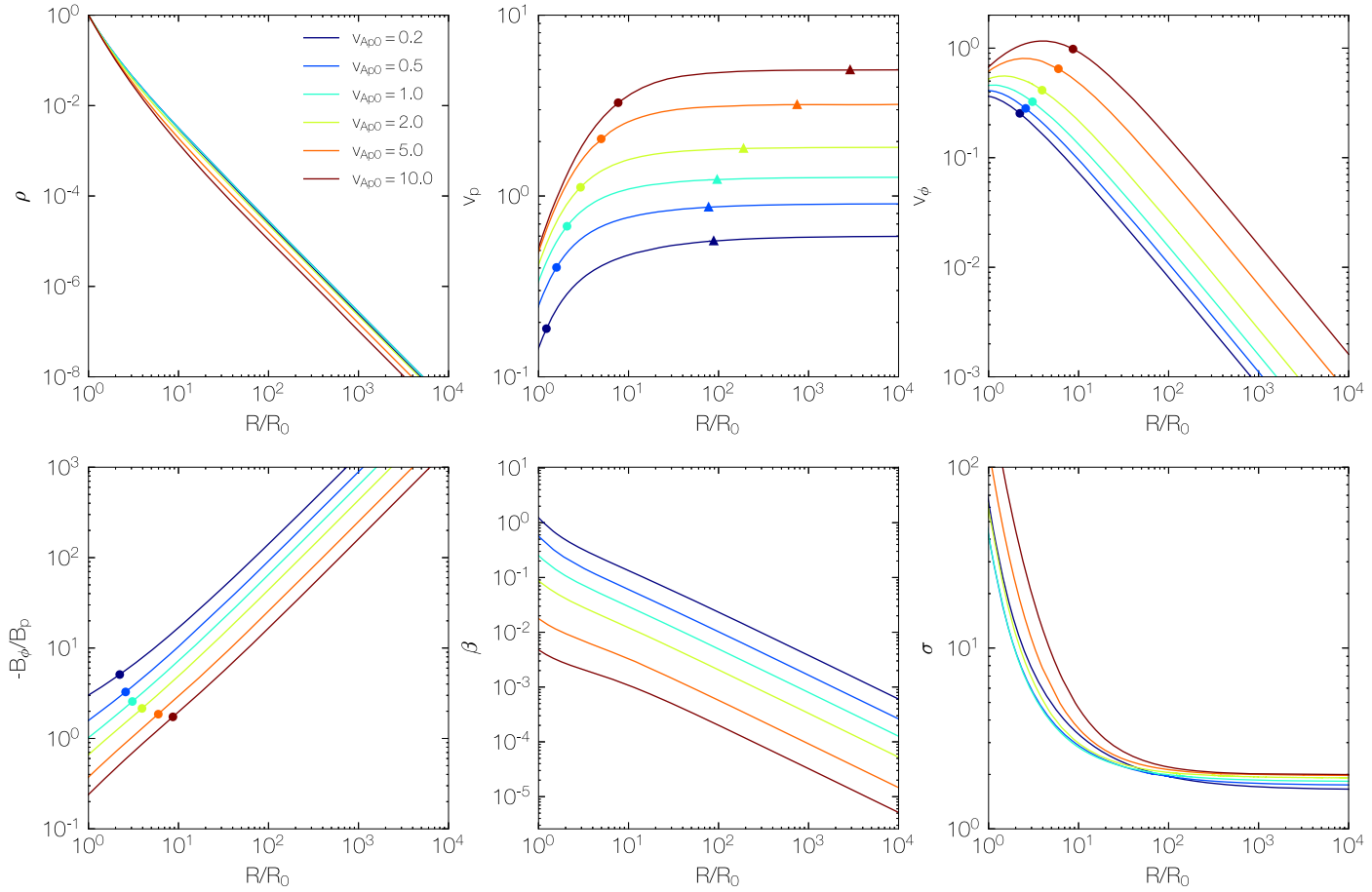

Figure 2. Profiles of density, poloidal and toroidal velocity, the ratio of the toroidal to the poloidal magnetic field, plasma β, and the ratio of the Poynting flux to the kinetic energy flux σ of the wind as a function of cylindrical radius R along the wind trajectory prescribed with $\theta = 45°$ to the rotational axis. Colors indicate various initial poloidal magnetic field strengths, with $v_{\rm Ap0}$ ranging from 0.2 to 10 $v_{\rm K0}$. Solid circles mark the Alfvén points, and triangles represent the fast magnetosonic points.

specific angular momentum, and the acceleration is driven by the toroidal magnetic pressure gradient. In our fiducial model, the gas is mainly in the case that is driven by the toroidal magnetic pressure gradient.

In the lower left panel, we display the ratio of the toroidal to the poloidal magnetic field. A minus sign is taken because the toroidal magnetic field has the opposite sign to the poloidal field both above and below the equatorial plane as a result of the disk rotation. Because $-B_\phi/B_{\rm p}$ scales approximately as $\propto R$, the toroidal field strength possesses a flatter slope than the poloidal field, with $B_\phi \propto R^{-1}$. The plasma β is computed by the ratio of gas pressure to magnetic pressure. Although $B_{\rm p}$ and B_ϕ are comparable at the wind base, the magnetic pressure is dominated by the toroidal component at large radii. The plasma β is then dominated by the profile of the sound speed because density and magnetic pressure have the same proportionality with R. The sound speed is proportional to $c_{\rm s}^2 \propto \rho^{\gamma-1}$ so that we obtain $\beta \propto c_{\rm s}^2 \propto R^{-0.8}$.

The conversion of Poynting flux to kinetic energy flux is shown in the lower right panel of Figure 2. Near the wind base, the magnetic energy dominates the kinetic energy. As the wind propagates outward, magnetic energy is converted into kinetic energy, yielding a decline in their ratio. Beyond the fast magnetosonic point, the ratio approaches an asymptotic value of $\sigma \sim 2$, as expected in Equation (31).

4.2. Dependence on the Poloidal Magnetic Field

To study the dependence of poloidal magnetic fields, we keep $c_{\rm s0}$ constant and vary $v_{\rm Ap0}$. Because the initial poloidal magnetic field strength is barely constrained, we explore a large domain by setting $v_{\rm Ap0} = 0.01 v_{\rm K0}$ and $v_{\rm Ap0} = 100 v_{\rm K0}$ to be the lower and upper limit (Figure 3). The lower values of $v_{\rm Ap0}$ (weak magnetic field strength) can be associated with the standard and normal evolution (SANE; Narayan et al. 2012) model that is referred to in hot accretion flow simulations, and higher values of $v_{\rm Ap0}$ (strong magnetic field strength) can be related to the magnetically arrested disk (MAD; Narayan et al. 2003) model.

In Figure 2 we show profiles of diagnostic physical quantities at various $v_{\rm Ap0}$ with nonconsecutive values from $0.2 v_{\rm K0}$ to $10 v_{\rm K0}$. The overall proportionality as a function of R of each physical quantity at large distances for different $v_{\rm Ap0}$ is very similar. Larger poloidal field strengths lead to fast poloidal velocities. The Alfvén points and fast magnetosonic points generally shift toward larger radii as poloidal fields are enhanced. The poloidal velocities all tend to approach an asymptotic value at large radii. At the fast magnetosonic point, the poloidal velocity mostly reaches its asymptotic value. The angular velocity in Figure 2 shows a transition from corotation to conserving specific angular momentum for strong poloidal fields. When the poloidal magnetic field is weak at the wind base, the magnetic tension is not able to sustain the corotation

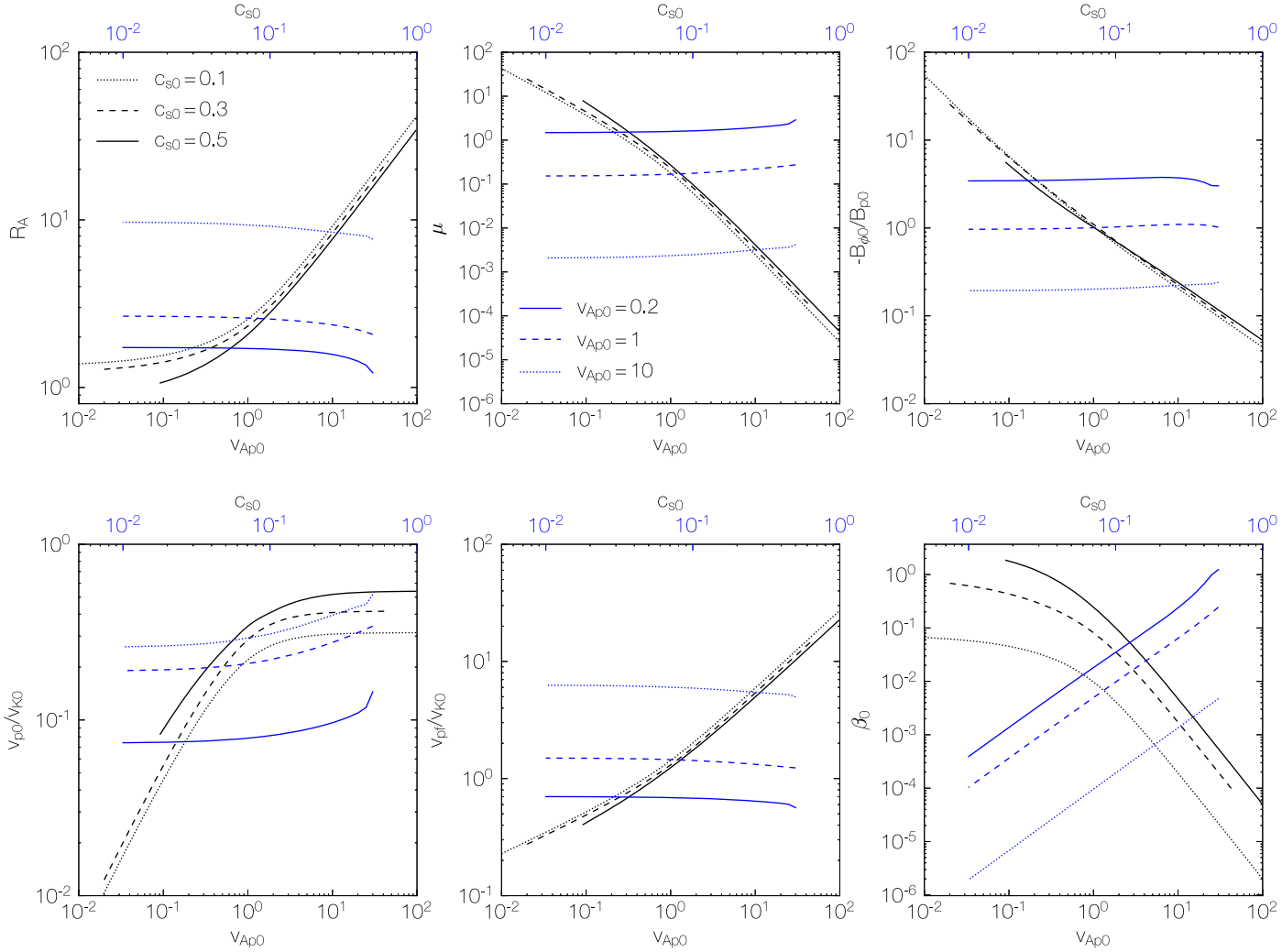

Figure 3. Alfvén radius, mass-loading parameter, ratio of the toroidal to the poloidal magnetic field strength, poloidal velocity at the wind base and at the fast magnetosonic point, and plasma β at the wind base as a function of the poloidal magnetic field $v_{\rm Ap0}$ (black curves) and temperature $c_{\rm s0}$ (blue curves) at the wind base. When we vary $v_{\rm Ap0}$, three temperature values are investigated, where $c_{\rm s0}=0.1$ (dotted), 0.3 (dashed), and 0.5 (solid). When we varyi $c_{\rm s0}$, three values of the poloidal field $v_{\rm Ap0}$ are investigated, where $v_{\rm Ap0}=0.2$ (solid), 1 (dashed), and 10 (dotted).

between the gas and the field line (see Section 4.4). The ratio of the toroidal to the poloidal magnetic field tends to be lower when the poloidal field strength is stronger at the launching point, as expected, and the plasma β drops with increasing $v_{\rm Ap0}$.

In Figure 3 we show in black curves the dependence of the poloidal field strength $v_{\rm Ap0}$ on the Alfvén point, the mass-loading parameter, the magnetic field strength ratio at the wind base, the poloidal velocity at the launching point and at the fast magnetosonic point, and the plasma β at the wind base. The field strength spans over 0.01–100 $v_{\rm K0}$. Shown in the upper left panel, the Alfvén point shifts toward large radii with $v_{\rm Ap0}$ and is boosted when $v_{\rm Ap0}\gtrsim 1$. The ejection index (Equation (26)), which is the ratio of the cumulative mass-loss rate to the wind-driven mass accretion rate, is directly related to the location of the Alfvén point. Taking representative values of $v_{\rm Ap0}=0.1$, 1, and 10, we find the corresponding ejection indices $\xi\approx 3$, 0.15, and 0.0086, respectively. Larger ejection indices correspond to more massive mass loading. As shown in the upper middle panel, the mass-loading factor is a decreasing function with $v_{\rm Ap0}$, hence an increasing function of ξ, as expected. The field strength ratio $|B_{\phi 0}/B_{\rm p0}|$ declines with $v_{\rm Ap0}$, which indicates that strong mass-loading leads to a fast development of the toroidal magnetic field because it is harder to enforce corotation with more massive winds so that the field line bends more.

The lower left panel of Figure 3 delineates the poloidal velocity at the wind base. In the domain of $v_{\rm Ap0}$ we investigated, the poloidal velocity at the footpoint $v_{\rm p0}$ spans over 0.01–0.5 $v_{\rm K0}$ with an increasing poloidal field strength. Small-scale 3D GRMHD simulations of hot accretion flows imply that near the surface, the poloidal velocity at each radius is about $0.2v_{\rm K}(r)$, where $v_{\rm K}(r)$ is the local Keplerian velocity (Y15). Their results are achieved by weighting through the mass flux of the wind at different radii because at each launching point r_0 the outflow is a combination of wind originating from $r<r_0$. We can approximately treat $0.2v_{\rm K}$ as the wind poloidal velocity launched at r_0 because wind that is launched at larger radii carries more mass flux, as concluded by fitting the simulation results, which gives $\dot{M}_{\rm wind}\propto r^s$ and $s\approx 1$. In Section 3 we reported that the poloidal velocity at the footpoint is not prescribed because the number of parameters to be given at the boundary are limited by requiring the wind solutions to pass through the slow and fast critical points. With

our fiducial wind temperature $c_{s0} = 0.5$ and the fiducial field strength at the wind base $v_{Ap0} = 0.2$, the poloidal velocity is $v_{p0} \approx 0.2 v_{K0}$, which is consistent with the GRMHD simulations. We also note that when $v_{Ap0} \gtrsim 1$, the poloidal velocity at the wind base approaches an asymptotic value of about $0.5 v_{K0}$.

The terminal velocity of the wind also deserves attention. It reaches a faster speed than the poloidal magnetic field as the wind base increases. The poloidal velocity can rise several times or be one order of magnitude higher than it is at the wind base. The fiducial model of $v_{Ap0} = 0.2$ reveals a terminal velocity of $v_{pf} \approx 0.5 v_{K0}$ ($\approx 0.016c$). Y15 trace the trajectory of the wind from 80 to $10^3 r_g$ to study the physical properties during the outward propagation of wind. They find that the poloidal velocity of the wind with opening angles $\theta \lesssim 30°$ shows an increase with distance, and it tends to remain constant since the launching point when $40° \lesssim \theta \lesssim 50°$. Their results are applicable to a radial extent close to the accretion disk (up to a few times $100 r_g$) where the corona region above the main disk body is rather turbulent, unlike the pure MHD model we adopted in this work.

It is immediately apparent that the plasma β_0 is a decreasing function with v_{Ap0}. As seen in the lower right panel of Figure 3, it ranges from unity down to 10^{-4} for $v_{Ap0} \in [0.01, 100]$ for the fiducial temperature $c_{s0} = 0.5$, and even lower when the temperature drops. Another diagnostic quantity of interest is the ratio of the Poynting flux to the kinetic energy flux σ. Although not shown in the figure, we report that the ratio of the Poynting flux to the kinetic energy flux is nearly a constant $\sigma \sim 2$ at large radii throughout the entire domain of v_{Ap0} and c_{s0} employed in Figure 3. This means that the values of the Alfvén velocity and the fast magnetosonic velocity are comparable toward large radii (Equation (31)).

4.3. Dependence on Temperature

We study the influence of the wind temperature at the launch point because it differs substantially for hot accretion flows and thin disks. In Figure 3 we first keep c_{s0} fixed throughout the domain of v_{Ap0} by adopting three representative values $c_{s0} = 0.1$, 0.3, and 0.5 v_{K0}. Then we vary c_{s0} at fixed values of $v_{Ap0} = 0.1$, 1, and 10 v_{K0}. We find that the wind properties do not show a strong dependency on the temperature at the footpoint, except for the plasma β_0.

The black curves in Figure 3 reveal that the influence of the launch point temperature on the wind evolution is modest. The enhanced wind temperature results in a smaller Alfvén radius, higher mass-loading, a faster launch velocity, and a slower terminal velocity. The magnetic field shows an equal partition between the poloidal and toroidal components for all three c_{s0} at $v_{Ap0} \sim 1$. With slopes of $|B_{\phi 0}/B_{p0}|$ varying slightly with different c_{s0}, the wind at the footpoint is generally more dominated by the toroidal field when $v_{Ap0} < 1$ and vice versa. When we fix v_{Ap0} at 0.2, 1, and 10 v_{K0}, the wind temperature c_{s0} from 0.01 to 0.5 v_{K0} is under investigation. Shown as blue curves in Figure 3, the diagnostic quantities generally vary slightly with c_{s0}, except for v_{Ap0} and β_0. The poloidal field v_{Ap0} shows a more prominent increase with $v_{Ap0} \gtrsim 1$. The plasma β_0 at the wind base is a strong function of c_{s0} because it is closely related to the gas pressure. The black and blue curves in the lower right panel of Figure 3 indicate that at fixed v_{Ap0}, higher temperature yields lower β_0, as expected.

4.4. Acceleration Mechanism

In this work, we aim to study how magnetism influences the dynamics of disk winds. The magnetically driving mechanism can be divided into two categories based upon the locus of the Alfvén point (Equations (24) and (25)). In general, with radii smaller than the Alfvén radius, the gas is accelerated mainly through magnetocentrifugal force where corotation is enforced. Beyond the Alfvén radius, gas conserves specific angular momentum and is accelerated thorugh the toroidal magnetic pressure gradient.

Physically, near the wind base, the poloidal magnetic field strength is reasonably large so that the magnetic pressure is stronger than the gas pressure or the ram pressure. The magnetic tension force persists, and the field line behaves like a rigid wire where gas is free to move along it, resembling the scenario of beads on a wire. The wind is enforced to corotate, with the field line sticking out of the disk surface. The enforced corotation causes the increase in centrifugal force with distance to sustain the outward acceleration. This regime is referred to as magnetocetrifugal force in driving outflows. Along the wind trajectory, the poloidal field strength drops toward large distances. The magnetocentrifugal acceleration will effectively stop when the ram pressure starts to exceed the magnetic pressure, and the corotation ceases to be valid because the magnetic tension force weakens. Meanwhile, the toroidal component of the field builds up as a result of the disk rotation and subsequently dominates its poloidal component. Then the flow is accelerated mainly through the toroidal magnetic pressure gradient.

The upper right panel in Figure 2 shows that with a strong poloidal magnetic field at the wind base ($v_{Ap0} \gtrsim 5$), corotation is enforced near the disk surface and the poloidal magnetic field dominates the toroidal component, as seen in the lower left panel. Close to the Alfvén radius, $|B_\phi/B_p|$ becomes higher than unity, and corotation ceases. Weak poloidal magnetic fields ($v_{Ap0} \lesssim 5$) possess a large $|B_\phi/B_p|$ at the wind base that do not even allow corotation.

A more intuitive understanding of the wind acceleration mechanism can be achieved by looking at the components of specific energy terms in the Bernoulli integral (Equation (12)), which is expressed in a frame that rotates with angular frequency ω. Rearranging Equation (12), we arrive at

$$\varepsilon = \frac{1}{2} v_p^2 + \frac{1}{2} v_\phi^2 + \Phi + h - v_\phi \omega R. \tag{33}$$

On the right-hand side of Equation (33), the terms correspond to the radial kinetic energy, the rotational energy, the gravitational potential, the enthalpy, and the centrifugal potential, respectively. In the upper panels of Figure 4, we show the components of the Bernoulli integral as a function of R at $v_{Ap0} = 0.2$, 1, and $10 v_{K0}$. In the limit of the weak poloidal field ($v_{Ap0} = 0.2 v_{K0}$), this suggests that the drop in enthalpy, rotational energy, and centrifugal potential compensates for the increase in gravitational potential and radial kinetic energy. More precisely, it is mainly the rapid decrease in enthalpy that offsets the quick growth of the gravitational potential, which is consistent with the results in Cui et al. (2019), where a pure hydrodynamic model is assumed. Toward the strong poloidal field limit ($v_{Ap0} = 10 v_{K0}$), the radial kinetic energy shows a more pronounced increase primarily as a result of the energy

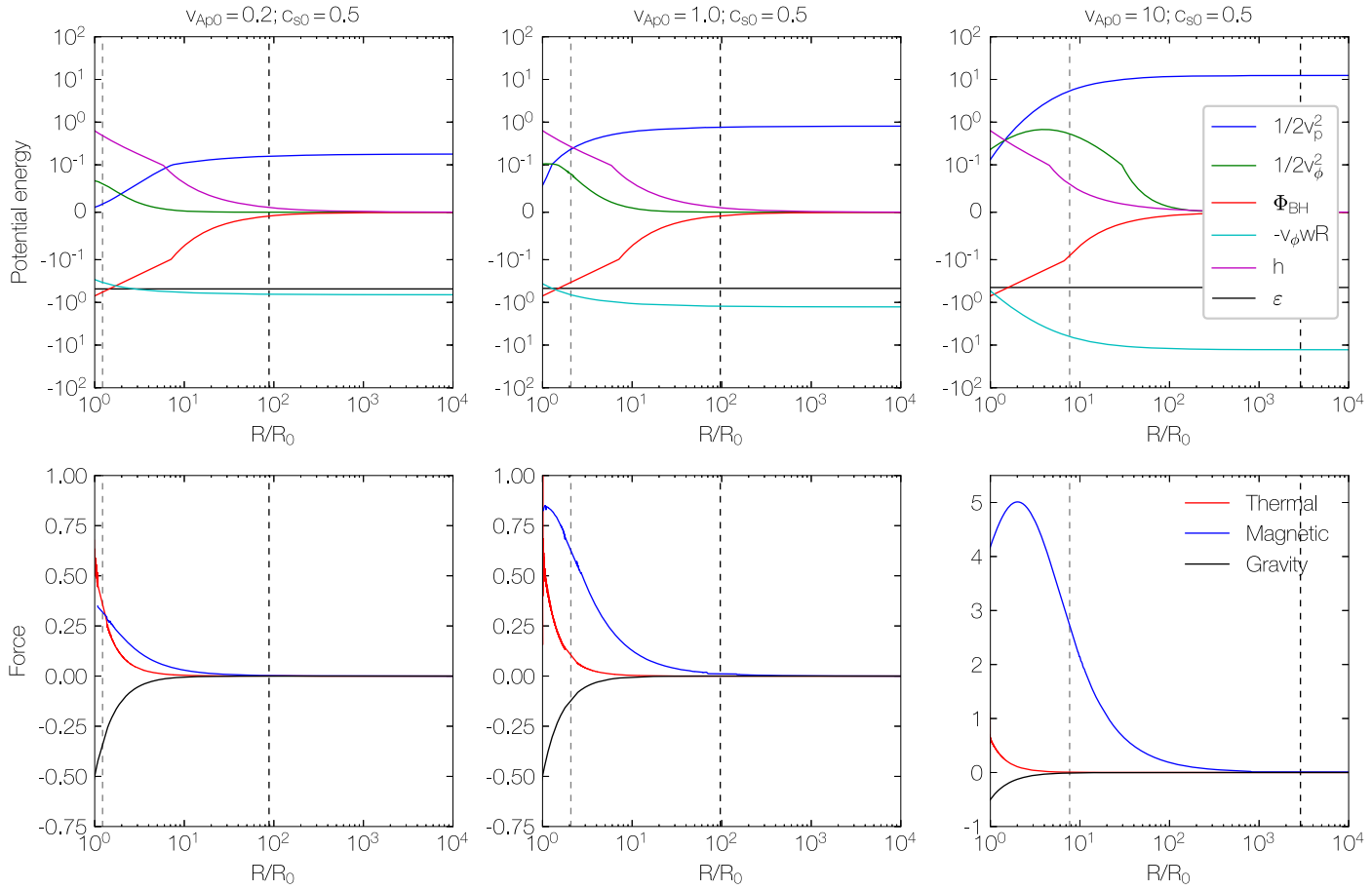

Figure 4. Components of potential energies and forces along the wind trajectory with varying $v_{\rm Ap0} = 0.2$ (first column), 1 (second column), 10 (third column), and fixed $c_{\rm s0} = 0.5$. Top panels: Bernoulli constant (ε) and components of potential energies, namely, radial kinetic energy ($1/2v_{\rm p}^2$), rotational energy ($1/2v_\phi^2$), black hole gravitational potential (Φ), enthalpy (h), and centrifugal potential ($-v_\phi \omega R$) as a function of R (Equation (33)). Bottom panels: components of forces, namely, thermal pressure gradient (red), magnetic pressure gradient (blue), and gravity (black) as a function of R (Equation (34)). The vertical dashed lines denote the Alfvén points (gray) and the fast magnetosonic points (black).

converted from the centrifugal potential. An intermediate poloidal field ($v_{\rm Ap0} = 1$) leads to an intermediate case.

It is noteworthy that the Bernoulli integral (Equation (12)) receives no contribution from magnetic forces because in the corotating frame, the total magnetic field $\boldsymbol{B}$ is parallel to the total velocity $\boldsymbol{v}$. Nonetheless, ultimately, the magnetic forces drive the outward propagation of the wind. We find that the magnetic term does involve the Bernoulli integral in its rest-frame expression (Section 2.2). To examine the effects of magnetism in driving disk winds, we write the equation of motion along the poloidal magnetic field as

$$\frac{dv_{\rm p}}{dt} = -\frac{1}{\rho}\frac{dP}{ds} - \frac{d\Phi}{ds} - \frac{1}{8\pi\rho}\frac{dB_\phi^2}{ds}, \tag{34}$$

where s is the length along the wind trajectory. The last term on the right-hand side is associated with the pressure gradient of the toroidal fields along the direction of wind propagation. The outward acceleration of the wind requires that the thermal and magnetic pressure gradient overcome gravity.

In the bottom panels of Figure 4 we decompose the poloidal forces into the thermal and magnetic pressure gradient, as well as gravity at different $v_{\rm Ap0}$ and fixed $c_{\rm s0} = 0.5 v_{\rm K0}$. In the limit of the weak poloidal field ($v_{\rm Ap0} = 0.2 v_{\rm K0}$), the forces exerted by the thermal and magnetic pressure gradient are comparable, with thermal pressure gradient being more pronounced before passing through the Alfvén point. The toroidal magnetic pressure gradient dominates the thermal pressure to drive outward acceleration when $v_{\rm Ap0} > 1$. The magnetic pressure gradient becomes overwhelming when the poloidal field at the wind base is strong, i.e., $v_{\rm Ap0} \gtrsim 10$, which results in a boost of the terminal velocity (Figure 3).

4.5. Dependence on Mass Loading

In Section 2.6 we presented (asymptotic) relations between diagnostic physical quantities (Equations (28)–(31)), namely, the Alfvén radius, the terminal velocity, the ratio of the magnetic field strength, the ratio of the Poynting flux to the kinetic energy flux, for which Equations (28)–(30) are derived in the case of the cold Weber & Davis wind model ($\theta = 90°$, $c_{\rm s0} = 0$). Our model differs from this by an inclined wind trajectory $\theta = 45°$ and $c_{\rm s0} = 0.1$, 0.3, and 0.5. Being more generalized, our results are compared to the derived relations to test whether they can still be obeyed.

The top panel in Figure 5 shows that high mass-loading (weak $v_{\rm Ap0}$) is associated with a small Alfvén radius, and accordingly, a high mass loss to the mass accretion rate. Our results perfectly match the relation in Equation (28), especially when $\mu \lesssim 0.1$ for all three $c_{\rm s0}$ is adopted. It seems that the relation holds for low mass-loading. When $\mu \gtrsim 0.1$, winds with different $c_{\rm s0}$ show deviations from the derived relation to

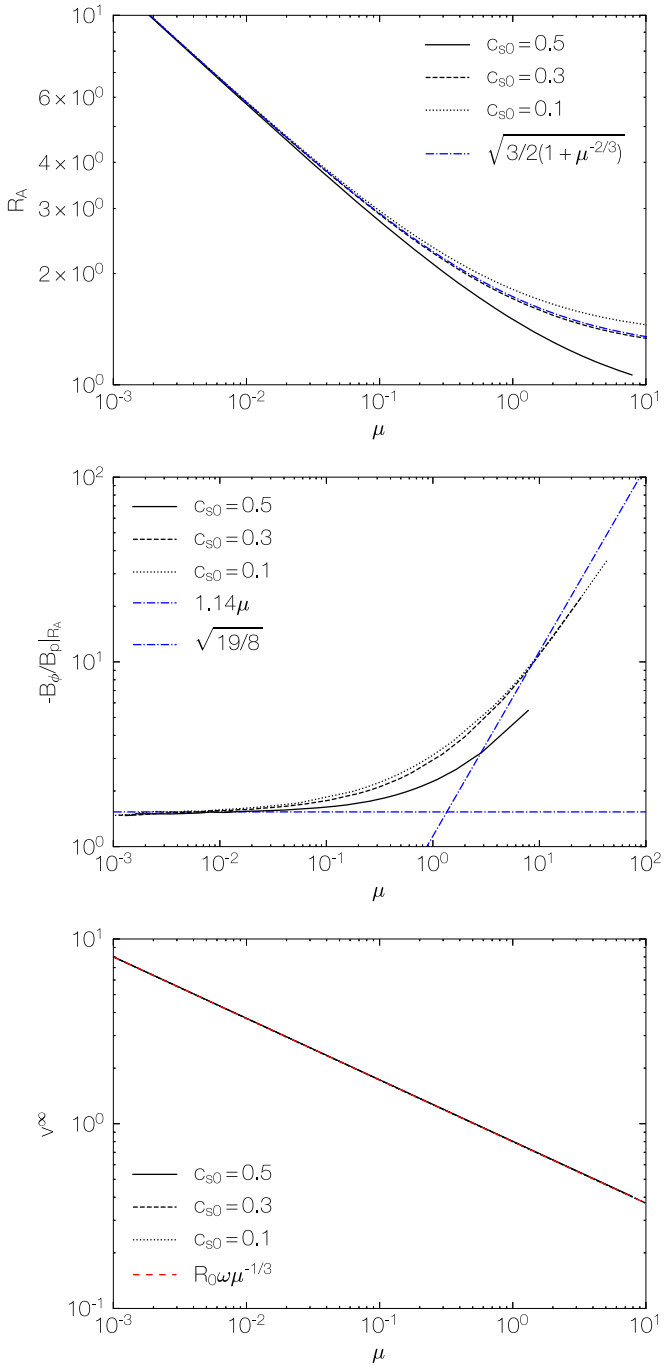

Figure 5. Diagnostic physical quantities as a function of mass-loading parameter μ at various wind base temperatures $c_{s0} = 0.5$ (solid black), 0.3 (dashed black), and 0.1 (dotted black). Top panel: loci of the Alfvén point as a function of the mass-loading parameter. Middle panel: ratio of the poloidal to the toroidal magnetic field strength at the Alfvén point. Bottom panel: wind terminal velocity as a function of μ. The dash–dotted blue curves in all panels denote the relation derived from the cold Weber & Davis wind model in Section 2.6.

different extents. R_A falls below expectation for $c_{s0} = 0.3$ and 0.5, but rises for $c_{s0} = 0.1$. A lower limit of $R_A = (3/2)^{1/2}$ is placed for high mass-loading by the cold wind model, while this is no longer valid for winds that possess finite temperature.

The middle panel of Figure 5 implies that high mass-loading results in a case that is more dominated by the toroidal magnetic field because it is more difficult to enforce that gas corotates with the field line when the outflow is massive. The horizontal asymptotic relation is strictly obeyed when $\mu \ll 1$ (strong v_{Ap0}) for all c_{s0}. In the weak poloidal field limit, colder winds show better consistency to the derived relation, while the curve of $c_{s0} = 0.5$ deviates more prominently from the asymptotic line. When μ is fixed, warmer winds tend to obtain lower $|B_\phi/B_p|_{R_A}$ values, because the Alfvén radius is closer to the wind base and $|B_\phi/B_p|_{R_A}$ is always an increasing function with radius.

In the bottom panel we show the terminal velocity as a function of mass loading μ. Despite the wind base temperature, all three models with various c_{s0} strictly satisfy the asymptotic relation. This is likely because our prescribed wind model, with an adiabatic index $\gamma = 1.4$, is cooled nearly adiabatically. Hence, the wind temperature drops rapidly with radius. At large distances, the wind is cold as in the model for the derived relation.

5. Parameter Study

We investigate the dependence of diagnostic physical quantities on the field line angular velocity (Section 5.1) and adiabatic index (Section 5.2) in this section. In Figure 6 we show two quantities of interest, namely R_A and v_{pf}, as a function of the poloidal magnetic field strength at the footpoint v_{Ap0}. The Alfvén point R_A directly relates to the mass loading and can be used to distinguish the regions dominated by magnetocentrifugal and toroidal magnetic pressure gradient. The terminal velocity v_{pf} shows the extent of the wind acceleration.

5.1. Dependence on the Field Angular Velocity

We compute the angular velocity of the field line using Equation (10) with small-scale accretion disk simulations. The θ dependence leads us to adopt a higher value of $\omega = 1$ to follow the trend of the solutions. In the lower left panel of Figure 6, we find that a higher field angular velocity results in a greater R_A and v_{pf}.

5.2. Dependence on the Adiabatic Index

The adiabatic index γ of the wind remains uncertain and is determined by the intricate interplay of thermal conduction, heating, and cooling. Accurate values can be obtained through numerical simulations by following the trajectory of the wind, which may introduce further complications to our MHD wind equations by varying its value along the field line. In the hydrodynamic case, $\gamma < 1.5$ is required to obtain transonic solutions when angular momentum is not taken into account.

For simplicity, we adopt a constant γ in the model and test adiabatic indices above and below our fiducial value. In the right panel of Figure 6, the wind solution is generally not a strong function of γ because R_A and v_{pf} do not show discernible variations when v_{Ap0} is greater than unity. When v_{Ap0} is lower than unity, larger adiabatic indices result in greater Alfvén radii. The reason is that the thermal pressure gradient is comparable to the magnetic force in driving winds at weak field strengths. The temperature that is determined by γ then plays an important role. As $v_{Ap0} > 1$, the magnetic force dominates the wind acceleration (see Figure 4) so that a slight variation in γ does not modify the solutions to a great extent.

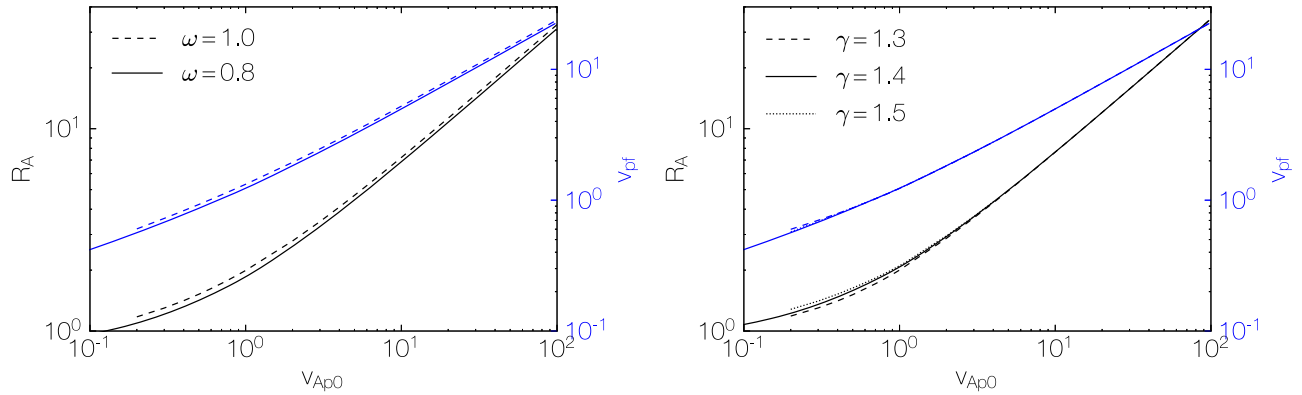

Figure 6. Alfvén radius R_A (black) and terminal velocity v_{pf} (blue) as a function of the poloidal field strength v_{Ap0} at various field line angular velocities $\omega \in \{0.8, 1\}$ and adiabatic indices $\gamma \in \{1.3, 1.4, 1.5\}$.

6. Conclusions and Discussion

6.1. Summary

In this work, we present an initial effort toward studying the dynamics of black hole accretion disk winds toward large radii. Disk winds are essential ingredients for AGN feedback in understanding the coevolution between the central supermassive black hole and the host galaxy. The limited dynamical range of small-scale accretion disk simulations does not allow us to study the kinematics of winds toward galaxy scales. In this work, we employ wind properties obtained in small-scale accretion disk simulations as our inner boundary conditions and adopt an analytic model to provide a simple but intuitive way to understand wind dynamics over a wider spatial range.

We construct 1D MHD equations following Webber & Davis (1967) in cylindrical coordinates. Four equations associated with four conserved quantities, including mass to magnetic flux, angular velocity of the field line, specific angular momentum, and specific energy (Equations (9)–(12)), are solved. The solution is requested to smoothly pass through the slow, Alfvén, and fast critical points. We do not impose the condition that all three critical points should have their loci beyond the wind base. Our fiducial model is set with parameters for winds from hot accretion flows, specifically, $c_{s0}/v_K = 0.5$, $v_{Ap0}/v_K = 0.2$, and $\omega/\Omega_K = 0.8$. The geometry of the poloidal magnetic field is prescribed as a straight line with a constant angle from the rotational axis ($\theta = 45°$), while the strength is described by the divergence-free condition. We summarize our main results as follows.

The physical quantities possess the following relations with cylindrical radius R as the wind passes the fast magnetosonic point:

$$\rho \propto R^{-2} \qquad v_p \propto \text{const.} \qquad v_\phi \propto R^{-1}$$
$$B_\phi \propto R^{-1} \qquad \beta \propto \rho^{\gamma-1}, \tag{35}$$

with the prescribed poloidal magnetic field $B_p \propto R^{-2}$. Moreover, we explore the dependence of the poloidal magnetic field at the wind base characterized by v_{Ap0} in a range from 0.01 to 100. The weak magnetic field case corresponds to the SANE model in accretion flow simulations, and the strong magnetic field case is associated with the MAD model. The Alfvén radius is a quickly increasing function with magnetization when v_{Ap0} is higher than unity, whereas the mass-loading parameter is a decreasing function of v_{Ap0}. Equal partition of $|B_{\phi 0}/B_{p0}|$ is achieved when v_{Ap0} is about unity, with smaller $|B_{\phi 0}/B_{p0}|$ toward large v_{Ap0}. The poloidal velocity at the footpoint v_{p0} is enlarged with v_{Ap0} but approaches an asymptotic value of $0.5v_{K0}$ when $v_{Ap0} > 1$. A faster terminal velocity v_{pf} is associated with a stronger v_{Ap0}, and the plasma β_0 is a decreasing function of magnetization, as expected. We further investigate the dependence of the temperature at the wind base c_{s0} from 0.01 to $0.5v_{K0}$, which shows modest effects on the physical quantities.

The wind acceleration mechanism is studied for different poloidal magnetic field strengths at the wind base. With strong poloidal fields $v_{Ap0} \gtrsim 5$, the corotation can be enforced close to the disk surface. Beyond the Alfvén radius, corotation ceases where the gas rotates by conserving specific angular momentum. Weak poloidal fields $v_{Ap0} \lesssim 5$ do not give rise to corotation. The decomposition of the Bernoulli constant reveals that with a weak poloidal field where $v_{Ap0} = 0.2$, it is chiefly the enthalpy that is converted into black hole potential energy, resembling the scenario in the pure hydrodynamic model. A strong poloidal field strength $v_{Ap0} = 10$ results in a fast rise of the radial kinetic energy, which is attributed to the conversion from the centrifugal potential. The decomposition of poloidal forces indicates that the thermal pressure gradient is comparable to the toroidal magnetic pressure gradient near the wind base at $v_{Ap0} = 0.2$, and the magnetic force dominates the acceleration for $v_{Ap0} \gtrsim 0.2$.

The dependence of diagnostic physical quantities on the mass-loading parameter μ is presented. Heavily loaded winds correspond to weakly magnetized winds ($v_{Ap0} < 1$). The Alfvén radius is a decreasing function of μ, while $|B_\phi/B_p|_{R_A}$ rises with it. The relations derived in the cold Weber & Davis model are generally obeyed for relatively cold winds in our model, whereas warmer winds show more deviations. The terminal velocity of the wind perfectly fits the derived relation, which seems not to be affected by the wind temperature. We deduce that this is caused by the nearly adiabatic cooling of the wind. The ratio of the Poynting flux to the kinetic energy flux toward large radii approaches an asymptotic value of $\sigma \sim 2$. The dependence on the field line angular velocity and the adiabatic index are explored as a function of v_{Ap0}. The Alfvén radius R_A and terminal velocity v_{pf} enlarge with higher field line angular velocity ω. The adiabatic index does not seem to affect the wind solution much, especially when $v_{Ap0} > 1$.

6.2. Discussion

6.2.1. Comparison with the Hydrodynamic Model

In the first paper of this series, a hydrodynamic wind model considering the black hole and galaxy potential was employed to study the wind dynamics toward large distances (Cui et al. 2019). The wind solution found in that work requires smooth passage through the sonic point, which is the only critical point in the hydrodynamic model. We demonstrate that the relations of the physical quantities as a function of cylindrical R are $\rho \propto R^{-2}$, $v_{\rm p} \propto$ const., and $v_\phi \propto R^{-1}$. The wind acceleration is attributed to the conversion of enthalpy into kinetic energy. For hot accretion flows, the radial velocity of wind is nearly constant ($\approx 0.2 v_{\rm K0}$) with the departure from the wind base.

When we include magnetism, we note that the hydrodynamic variables share the same proportionalities with R as those in the hydrodynamic model. The wind is accelerated by both thermal pressure and magnetic force for weak magnetization ($v_{\rm Ap0} \sim 0.2$), where the toroidal magnetic pressure gradient dominates the magnetic force. For strong magnetization ($v_{\rm Ap0} > 1$), thermal pressure is not important and the acceleration is attributed to the magnetocentrifugal force near the surface and to the magnetic pressure gradient beyond the Alfvén radius. This causes the terminal velocity for the magnetized wind to reach $v_{\rm pf} = 0.5 v_{\rm K0}$ ($\approx 0.016c$) for the fiducial model where $v_{\rm Ap0} = 0.2$, and increases to $v_{\rm pf} = v_{\rm K0} (\approx 0.03c)$ and $v_{\rm pf} = 5 v_{\rm K0} (\approx 0.15c)$ for $v_{\rm Ap0} = 1$ and 10, respectively (Figure 3).

6.2.2. Caveats

One limitation of this work is that we do not include the galaxy potential in the MHD equations. As the wind propagates over the accretion scales, the gravitational potential from the galaxy will play a role against its outward acceleration. This additional potential will be involved in the Bernoulli integral. Nevertheless, our hydrodynamic results imply that the galaxy potential does not significantly affect the wind solution when reasonable parameters at the wind-launching point are adopted. With the complexity of solving for MHD equations, the galaxy potential is thereby temporarily excluded in this work for the sake of simplicity.

Another caveat comes from the collimation of the wind. To confine the momentum flux of the outflow, it can be either compressed by an external medium that is dominated by gas pressure or by the hoop stress associated with the magnetic tension of the toroidal magnetic field. However, the kink instability takes place with the presence of a predominating toroidal field. Once the instability sets in, the collimation provided by the hoop stress is mitigated (Eichler 1993). Rather than collimated by the toroidal pinching force, the poloidal disk magnetic field is suggested to preserve the collimation (Spruit et al. 1997). The winds are expected to experience the confinement via the mechanisms mentioned above. The collimation modifies the trajectory of the wind such that the geometry and strength of the poloidal magnetic field would be different. However, previous work has proved that the wind properties are not sensitive to the field geometry (Bai et al. 2016). To properly deal with the collimation of the flow, the force balance in the (R, z)-plane perpendicular to the poloidal magnetic field should be considered (e.g., Sakurai 1985; Grad-Shafranov equation). In this case, the solutions obtained for a fixed poloidal magnetic field are still valid, but we should interpret the results in terms of the yet-to-be-determined poloidal field.

We thank the anonymous referee for valuable comments on the MHD theory. This work is supported in part by the National Key Research and Development Program of China (grant No. 2016YFA0400704), the Natural Science Foundation of China (grants 11573051, 11633006, 11650110427, 11661161012), the Key Research Program of Frontier Sciences of CAS (No. QYZDJSSW-SYS008), and the Astronomical Big Data Joint Research Center co-founded by the National Astronomical Observatories, Chinese Academy of Sciences and the Alibaba Cloud.

ORCID iDs

Can Cui https://orcid.org/0000-0003-3180-0038
Feng Yuan https://orcid.org/0000-0003-3564-6437

References

Anderson, J. M., Li, Z.-Y., Krasnopolsky, R., et al. 2005, ApJ, 630, 945
Bai, X.-N., Ye, J., Goodman, J., et al. 2016, ApJ, 818, 152
Begelman, M. C., McKee, C. F, & Shields, G. A. 1983, ApJ, 271, 70
Blandford, R. D., & Begelman, M. C. 1999, MNRAS, 303, L1
Blandford, R. D., & Payne, D. G. 1982, MNRAS, 253, 873
Blandford, R. D., & Znajek, R. L. 1977, MNRAS, 179, 433
Bu, D.-F., & Mosallanezhad, A. 2018, A&A, 615, 35
Cannizzo, J. K., & Pudritz, R. E. 1988, ApJ, 327, 840
Cao, X. W. 2014, ApJ, 783, 51
Cao, X. W., & Spruit, H. C. 1994, A&A, 287, 80
Choi, E., Ostriker, J. P., Naab, T., & Johansson, P. H. 2012, ApJ, 754, 125
Ciotti, L., Ostriker, J. P., & Proga, D. 2010, ApJ, 717, 708
Ciotti, L., Pellegrini, S., Negri, A., & Ostriker, J. P. 2017, ApJ, 835, 15
Clarke, C. J., & Alexander, R. D. 2016, MNRAS, 460, 3044
Contopoulos, J. 1995, ApJ, 450, 616
Contopoulos, J., & Lovelace, R. V. E. 1994, ApJ, 429, 139
Cui, C., Yuan, F., & Li, B. 2019, ApJ, 890, 80
Eichler, D. 1993, ApJ, 419, 111
Eisenreich, M., Naab, T., Choi, E., Ostriker, J. P., & Emsellem, E. 2017, MNRAS, 468, 751
Everett, J. E. 2005, ApJ, 631, 689
Ferreira, J. 1997, A&A, 319, 340
Ferreira, J., & Pelletier, G. 1995, A&A, 295, 807
Font, A. S., McCarthy, I. G., Johnstone, D., et al. 2004, ApJ, 607, 890
Fukumura, K., Kazanas, D., Contopoulos, I., et al. 2010, ApJ, 715, 636
Kato, S. X., Kudoh, T., & Shibata, K. 2002, ApJ, 565, 1035
Konigl, A. 1989, ApJ, 342, 208
Krasnopolsky, R., Li, Z.-Y., & Blandford, R. 1999, ApJ, 526, 631
Kudoh, T., & Shibata, K. 1997, ApJ, 474, 362
Li, J., Ostriker, J., & Sunyaev, R. 2013, ApJ, 767, 105
Li, Z.-Y. 1995, ApJ, 444, 848
Li, Z.-Y. 1996, ApJ, 465, 855
Lovelace, R. V. E., Berk, H. L., & Contopoulos, J. 1991, ApJ, 379, 696
Luketic, S., Proga, D., Kallman, T. R., Raymond, J. C., & Miller, J. M. 2010, ApJ, 719, 515
Lynden-Bell, D. 1996, MNRAS, 279, 389
Lynden-Bell, D. 2003, MNRAS, 341, 1360
Murray, N., Chiang, J., Grossman, S. A., & Voit, G. M. 1995, ApJ, 451, 498
Narayan, R., Igumenshchev, I. V., & Abramowicz, M. A. 2003, PASJ, 55, 69
Narayan, R., SÄdowski, A., Penna, R. F., et al. 2012, MNRAS, 426, 3241
Narayan, R., & Yi, I. 1994, ApJL, 428, L13
Nomura, M., & Ohsuga, K. 2017, MNRAS, 465, 2873
Ogilvie, G. I. 2016, JPlPh, 82, 205820301
Ostriker, E. C. 1997, ApJ, 486, 291
Ostriker., J. P., Choi, E., Ciotti, L., et al. 2010, ApJ, 722, 642
Ouyed, R., & Pudritz, R. E. 1997a, ApJ, 482, 712
Ouyed, R., & Pudritz, R. E. 1997b, ApJ, 484, 794
Ouyed, R., & Pudritz, R. E. 1999, MNRAS, 309, 233
Pelletier, G., & Pudritz, R. E. 1992, ApJ, 394, 117
Porth, O., & Fendt, C. 2010, ApJ, 709, 1100
Proga, D. 2003, ApJ, 585, 406
Proga, D., & Kallman, T. R. 2002, ApJ, 543, 455

Proga, D., & Kallman, T. R. 2004, ApJ, 616, 688
Proga, D., Stone, J. M., & Kallman, T. R. 2000, ApJ, 543, 686
Pudritz, R. E., & Norman, C. A. 1983, ApJ, 274, 677
Pudritz, R. E., & Norman, C. A. 1986, ApJ, 301, 571
Pudritz, R. E., Rogers, C. S., & Ouyed, R. 2006, MNRAS, 365, 1131
Romanova, M. M., Ustyugova, G. V., & Koldoba, A. V. 1997, ApJ, 482, 708
Sakurai, T. 1985, ApJ, 152, 121
Sakurai, T. 1987, PASJ, 39, 821
Shibata, K., & Uchida, Y. 1986, PASJ, 38, 631
Spruit, H. C. 2016, ASIC, 477, 249
Spruit, H. C., Foglizzo, T., & Stehle, R. 1997, MNRAS, 288, 333
Stone, J. M., & Norman, M. L. 1994, ApJ, 433, 746
Uchida, Y., & Shibata, K. 1985, PASJ, 37, 515
Ustyugova, G. V., Koldoba, A. V., Romanova, M. M., et al. 1995, ApJ, 439, 39
Ustyugova, G. V., Koldoba, A. V., Romanova, M. M., et al. 1999, ApJ, 516, 221
Vlahakis, N., Tsinganos, K., Sauty, C., et al. 2000, MNRAS, 318, 417
Waters, T. R., & Proga, D. 2012, MNRAS, 426, 2239
Waters, T. R., & Proga, D. 2018, MNRAS, 481, 2628
Webber, E. J., & Davis, J. R. L. 1967, ApJ, 148, 217
Weinberger, R., Springel, V., Hernquist, L., et al. 2017, MNRAS, 465, 3291
Yoon, D., Yuan, F., Gan, Z., et al. 2018, ApJ, 864, 6
Yoon, D., Yuan, F., Ostriker, J. P., & Ciotti, L. 2019, ApJ, 885, 16
Yuan, F., Bu, D., & Wu, M. 2012a, ApJ, 761, 130
Yuan, F., Gan, Z., Narayan, R., et al. 2015, ApJ, 804, 101
Yuan, F., Quataert, E., & Narayan, R. 2003, ApJ, 598, 301
Yuan, F., Wu, M., & Bu, D. 2012b, ApJ, 761, 129
Yuan, F., Yoon, DooSoo., Li, Ya-Ping., et al. 2018, ApJ, 857, 121
Zanni, C., Ferrari, A., & Rosner, R. 2007, A&A, 469, 811